

Precipitation and Phase Transformations in 2101 Lean Duplex Stainless Steel During Isothermal Aging



JEAN-YVES MAETZ, SOPHIE CAZOTTES, CATHERINE VERDU,
and XAVIER KLEBER

The effect of isothermal aging at 963 K (690 °C) on the microstructure of a 2101 lean duplex stainless steel, with the composition Fe-21.5Cr-5Mn-1.6Ni-0.22N-0.3Mo, was investigated using a multi-technique and multi-scale approach. The kinetics of phase transformation and precipitation was followed from a few minutes to thousands of hours using thermoelectric power measurements; based on these results, certain aging states were selected for electron microscopy characterization. Scanning electron microscopy, electron back-scattered diffraction, and transmission electron microscopy were used to quantitatively describe the microstructural evolution through crystallographic analysis, chemical analysis, and volume fraction measurements from the macroscopic scale down to the nanometric scale. During aging, the precipitation of $M_{23}C_6$ carbides, Cr_2N nitrides, and σ phase as well as the transformation of ferrite into austenite and austenite into martensite was observed. These complex microstructural changes are controlled by Cr volume diffusion. The precipitation and phase transformation mechanisms are described.

DOI: 10.1007/s11661-015-3215-7

© The Minerals, Metals & Materials Society and ASM International 2015

I. INTRODUCTION

THE industrial application of duplex stainless steels (DSS) is increasing, mainly in the chemical, petrochemical, marine, and nuclear industries.^[1] Indeed, this family of steels combines good mechanical and corrosion resistance properties due to a δ -ferrite/ γ -austenite phase ratio close to 1. DSS is usually delivered in the annealed two-phase condition after a solution treatment is performed at 1323 K to 1373 K (1050 °C to 1100 °C). Undesirable phases, such as the σ phase, carbides, nitrides, and other intermetallic phases, are known to precipitate in DSS during aging, leading to a dramatic deterioration of the mechanical and corrosion properties.^[1,2] In standard and super DSS, the embrittlement nose is caused by the formation of the Cr-Mo-rich σ phase and occurs in as few as several minutes of aging at 1173 K (900 °C).^[3,4] The σ phase precipitates mainly in δ through an eutectoid transformation of δ into σ and γ_2 -secondary austenite.^[3,5] However, carbides and nitrides precipitate first in this range of temperatures. During aging of 2205 DSS (UNS S32205), Lee *et al.*^[6] observed the migration of the δ/γ interface boundary into δ through the lamellar growth of $M_{23}C_6$ carbides and γ_2 followed by σ -phase precipitation. Chen *et al.*^[7] reported that the σ phase preferentially nucleates at the interfaces between preformed $M_{23}C_6$ and δ at γ/δ phase boundaries. When using N as an alloying element in

DSS, the precipitation of Cr_2N nitrides is likely to occur along δ/γ and δ/δ interfaces.^[3] Ramirez *et al.*^[8,9] investigated five ferritized DSS reheated at 1173 K to 1473 K (900 °C to 1200 °C) for a few seconds and proposed a model to describe the migration of the γ/δ interface due to Cr_2N precipitation. Cr_2N and γ_2 grow together in δ until the diffusion of the heavy nitride forming elements, such as Cr, Mo, and V, limits the Cr_2N growth and allows γ_2 to grow alone. The Cr_2N nitrides remain on the γ/γ_2 interface and dissolve as aging progresses.

Since the late 1990s, significant studies have been devoted to the development of lean DSS, a family of stainless steels that combines the good mechanical properties characteristic of DSS with the corrosion resistance of standard austenitic stainless steels.^[10,11] The 2101 DSS was mainly designed for light-weight constructions and using this grade instead of the dominating stainless steel grades, typified by the austenitic AISI 304 (EN 1.4301), allows significant weight-saving. As a fact, the 2101 DSS is an economical alternative to these standard austenitic stainless steels. Compared with other DSS, the corrosion resistance and cost-processing of the 2101 DSS are usually weaker, as the Ni and Mo contents are lower. It is compensated by higher N and Mn contents to stabilize γ and maintain an equivalent amount of γ and δ phases. Nowadays, the 2101 DSS is well established in the market, as a general and multipurpose stainless construction steel,^[11] used for various applications such as tanks and pipelines, for which the use of 2205 DSS would be over-specified from a corrosion perspective.^[1,10,11]

Investigations on the microstructural evolution of lean DSS are not as extensive as for 2205 and 2507 DSS. As the composition of lean DSS differs from that of conventional DSS, a different aging behavior is

JEAN-YVES MAETZ, Postdoctoral Fellow, SOPHIE CAZOTTES, Assistant Professor, and CATHERINE VERDU and XAVIER KLEBER, Professors, are with the Université de Lyon, INSA Lyon, MATEIS, UMR CNRS 5510, 69621 Villeurbanne, France. Contact e-mail: jean-yves.maetz@ubc.ca

Manuscript submitted March 2, 2015.

Article published online November 6, 2015

expected. It is accepted that the embrittlement nose of 2101 lean DSS is approximately 923 K to 1023 K (650 °C to 750 °C) because of the precipitation of Cr₂N and M₂₃C₆ at δ/γ and δ/δ interfaces, which begins after a few minutes of aging.^[12–14] The kinetics of σ -phase precipitation is expected to be more sluggish than in standard and super DSS due to the lower Cr and Mo contents^[10,14] and σ -phase is generally observed after several tens of hours of aging at 973 K (700 °C).^[13,15] However studies on the σ -phase fraction evolution and the thermal stability of the various phases during long-term aging have been relatively limited; *e.g.*, Calliari *et al.*^[16] observed α' martensite in 2101 DSS after 25 minutes of aging at 1023 K (750 °C) followed by quenching, which has not been reported in other studies.

The present paper is devoted to understanding the precipitation mechanisms and phase transformations in a 2101 commercial lean DSS (EN 1.4162, UNS S32101) during isothermal aging at 963 K (690 °C) in the embrittlement nose temperature range. A multi-technique and multi-scale approach has been developed to accurately characterize the microstructural changes. The kinetics of the microstructural evolution during aging was followed using thermoelectric power (TEP) measurements; based on these results, certain aging states were selected and characterized using electron microscopy. Scanning electron microscopy (SEM), electron back-scattered diffraction (EBSD), and transmission electron microscopy (TEM) were used to investigate the crystallographic features, structural stability, and chemical composition of the phases and to quantitatively describe their growth. Scenarios of the microstructural evolution are proposed for each interface, γ/δ , δ/δ , and γ/γ , with a description of the diffusion of alloying elements controlling the phase transformations.

II. EXPERIMENTAL

A. Material and Heat Treatments

The as-received material is a 3-mm-thick hot-rolled sheet of commercial LDX 2101[®] duplex stainless steel developed by Outokumpu. The final step of the industrial process was a solution annealing at approximately 1323 K (1050 °C) followed by rapid quenching.^[2,10] To study the effect of aging on the microstructure of the 2101 DSS, isothermal aging was performed at 963 K (690 °C) in a conventional chamber furnace from 2 minutes up to 3600 hours followed by water quenching. These heat treatments were interrupted for TEP and hardness measurements (6 measurements, load of 0.2 kg), which were performed at room temperature; the reported aging time represents the effective cumulative time in the furnace, set at the aging temperature T . The electron microscopy samples were heat treated to the selected aging time at once.

B. Thermoelectric Power Measurements

The TEP (or the Seebeck coefficient, $\mu\text{V}\cdot\text{K}^{-1}$) is particularly well-suited to follow microstructural

changes during aging^[17,18] because this physical property is highly sensitive to defects in metals and especially to composition changes of the solute.^[19] For single-phase low-alloyed metals, the equation below is a good approximation of the TEP “S”

$$S = S_0 + \sum_i \Delta S_i \quad \text{and} \quad \Delta S_i = K_i C_i$$

Here, S_0 is the TEP of the pure metal, ΔS_i is the TEP contribution of the alloying element “i,” and C_i is the concentration of the alloying element “i” in the solid solution. K_i is a coefficient that is inherent to each element “i” in the solid solution of a pure metal. In low-alloyed iron, K_i is slightly positive ($K_i > 0$) for Cr^[20] and strongly negative ($K_i \ll 0$) for N and C,^[17,21,22] whereas in austenite, limited data are available except for the data provided by Lasseigne *et al.*,^[23] who measured a slight negative effect of N on the TEP of an austenitic stainless steel. For multiphase alloys, Kléber *et al.*^[24] demonstrated that the TEP is proportional to the volume fractions of the phases, provided that the phases exhibit similar electrical properties.

For complex alloys such as 2101 DSS, different mechanisms may occur simultaneously during aging and interact with each other. Consequently, TEP measurements during aging are used in this study to qualitatively follow the kinetics of precipitation and phase transformations.

The TEP was measured at 293 K (20 °C) for specimens with sizes of approximately $1 \times 3 \times 60 \text{ mm}^3$ with an apparatus developed in the laboratory.^[21] The TEP was measured relative to a copper reference. To plot the TEP curves, only the TEP evolution with aging time $\Delta S = S_t - S_{t=0}$ was considered and not the absolute TEP. $S_{t=0}$ (approximately $-0.85 \mu\text{V}\cdot\text{K}^{-1}$) is the TEP of the as-received 2101 DSS relative to that of the copper reference, and S_t is the TEP of the aged sample after the cumulative time “ t ” at 963 K (690 °C). Six measurements were performed for each time step, and the maximum standard deviation observed for the means was $0.02 \mu\text{V}\cdot\text{K}^{-1}$.

C. Microscopy

The as-received 2101 DSS samples were prepared for optical microscopy by mechanical polishing followed by etching in a $0.1 \text{ g}\cdot\text{mL}^{-1}$ KOH electrolyte at 5 V for approximately 15 seconds. Ferrite appears darker than austenite,^[15] making phase fraction measurement possible on large areas from optical micrographs (75 images of $640 \times 480 \mu\text{m}^2$). Only the as-received sample was characterized by means of optical microscopy. The as-received 2101 DSS and the samples aged at 963 K (690 °C) for 15 minutes, 2 hours, 10, 24, 120, 350, and 3300 hours were prepared for SEM and EBSD. A colloidal silica suspension was used for the final polishing step after SiC grinding papers and diamond polishing up to $1 \mu\text{m}$.

An FEG ZEISS SUPRA[™] VP55 microscope was used for the SEM analysis, equipped with an Oxford Instrument EBSD camera and with HKL Channel Five and AztecHKL softwares for the EBSD analysis. The

minimum angle grain boundary disorientation was set as 5 deg for map representation and analysis. The crystallographic structures entered in the software for the Cr₂N and the σ phase are the trigonal structure of space group P $\bar{3}$ 1m with lattice parameters $a = 0.4752$ nm and $c = 0.4429$ nm^[25] and the body-centered tetragonal structure of the space group P4₂/mnm with lattice parameters $a = 0.880$ nm and $c = 0.454$ nm,^[26] respectively. M₂₃C₆ have an fcc-crystal structure with a lattice parameter $a = 1.065$ nm,^[27] which is approximately three times larger than the lattice parameter of austenite ($a_\gamma = 0.36$ nm). Therefore, the M₂₃C₆ precipitates were not detected during EBSD acquisition and were indexed as austenite. Bcc-martensite (α') is indexed as ferrite by EBSD because these phases have very similar lattice structures ($a_\delta = 0.287$ nm). However, a contrast difference between δ and α' was observed in the band slope and kernel average misorientation (KAM) EBSD maps^[28] due to the local amount of strain induced by the γ to α' transformation. The grain morphology and this contrast difference were used to distinguish α' from δ and to deduce the volume fractions of both phases.

The volume fractions of the phases (γ , σ , δ , and α') were estimated from the surface measurements on the EBSD maps for the different aging states. Depending on the aging state, between 2 and 14 maps were recorded in various zones for a total surface of 0.2 to 1.5 mm². The precipitate surface fractions were estimated from contrast analysis of 25 random back-scattered-electron-SEM images of $29 \times 38 \mu\text{m}^2$, where the precipitates appear darker than the matrix. The σ -phase fraction, which appears lighter than the matrix in BSE-SEM, was also determined from BSE-SEM image analysis; the results are in good agreement with the σ -fraction measured by EBSD.

TEM was used on two types of samples: thin foils for bulk samples and carbon replicas deposited on copper grids for precipitate observations of the early aging stage. Thin foils were prepared from thick discs thinned to 50 μm by mechanical polishing and twin-jet-polishing in a solution of 10 pct perchloric acid–90 pct methanol between 248 K and 258 K (–25 °C and –15 °C) at a 40 V etching potential using a Gatan Tenupol device. Final polishing was performed with a Gatan precision ion polishing system (PIPS). For replica preparation, both the first chemical attack during 1 minute and the matrix dissolution after the carbon film deposition were performed using a 10 g·L^{–1} picric acid, 5 pct HCL, and 95 pct methanol solution. JEOL 200CX and JEOL 2010F microscopes with accelerating voltages of 200 kV were used for the TEM analyses. The orientation relationships (ORs) between Cr₂N and the two phases of the matrix (γ and δ) were investigated using TEM selected area diffraction (SAD) and EBSD using

pole figures, while only TEM-SAD was used to determine the ORs between M₂₃C₆ and the matrix phases. The ORs among γ , δ , and α' were determined using EBSD.

The grain size of the as-received material was determined using EBSD from 14 random EBSD maps for a total surface of 1.5 mm². The diameters of the grains were estimated from the surface measurements, which were plotted as a function of their numerical density and fitted with a log-normal law to determine the mean diameter and the corresponding standard deviation. The precipitate size was identically determined for each aged state from the analysis of the 25 BSE-SEM images. Due to the precipitate size, these results were completed using TEM-high-angle annular dark field (HAADF) image analysis for the sample aged for 15 minutes.

III. RESULTS

A. Microstructure of the As-received Material

The measured chemical composition of the investigated 2101 DSS in the as-received condition is listed in Table I and the typical microstructure of the normal section is shown in Figure 1(a). It consists of γ and δ grains and no other significant phases were identified in this state. Elongated γ islands composed of small equiaxed grains are embedded in the large coarse-grained δ matrix due to the solid nucleation and growth of γ in δ .^[2] On the transverse section, a banded structure of γ and δ islands is observed. Classic Kurdjumov–Sachs (K–S) or Nishiyama–Wassermann (N–W) ORs are typical of the fcc to bcc transformation^[29,30] but in most cases, no particular ORs at the γ/δ interfaces were observed using EBSD. More than 95 pct of the grain boundaries shown in the figures have high angle disorientation (>15 deg), in both phases. A δ/γ phase ratio close to 1 was measured by EBSD, with 52 ± 3 pct δ and 48 ± 3 pct γ . Similar results were obtained by optical image analysis and global magnetic measurements, as γ is paramagnetic and δ is ferromagnetic. The mean diameter of the γ grains is $6 \pm 4 \mu\text{m}$, while the δ grain size follows a bimodal lognormal distribution with mean diameters of 3 ± 2 and $13 \pm 8 \mu\text{m}$, respectively.

The chemical compositions of γ and δ in the as-received material were measured by microprobe and are listed in Table II. As expected, δ is enriched in α stabilizing elements^[31] such as Cr, Mo, and Si while γ is enriched in γ stabilizing elements, such as Ni, Mn, and especially N. Because carbon is too light to be measured accurately by microprobe, the Thermo-Calc[®] software was used to estimate the carbon content of both phases. The temperature of 1400 K (1123 °C) is used, for which the simulated equilibrium phase fraction of γ and δ

Table I. Chemical Composition of the Studied 2101 DSS (Weight Percent) Measured by Combustion–Conductimetry for N, Combustion–Absorption for C, Atomic Emission Spectroscopy for Al, and X-ray Fluorescence for the Others Elements

C	N	Ni	Cr	Mn	Si	Mo	Cu	V	Fe
0.023	0.22	1.63	21.54	4.98	0.69	0.29	0.31	0.085	balance

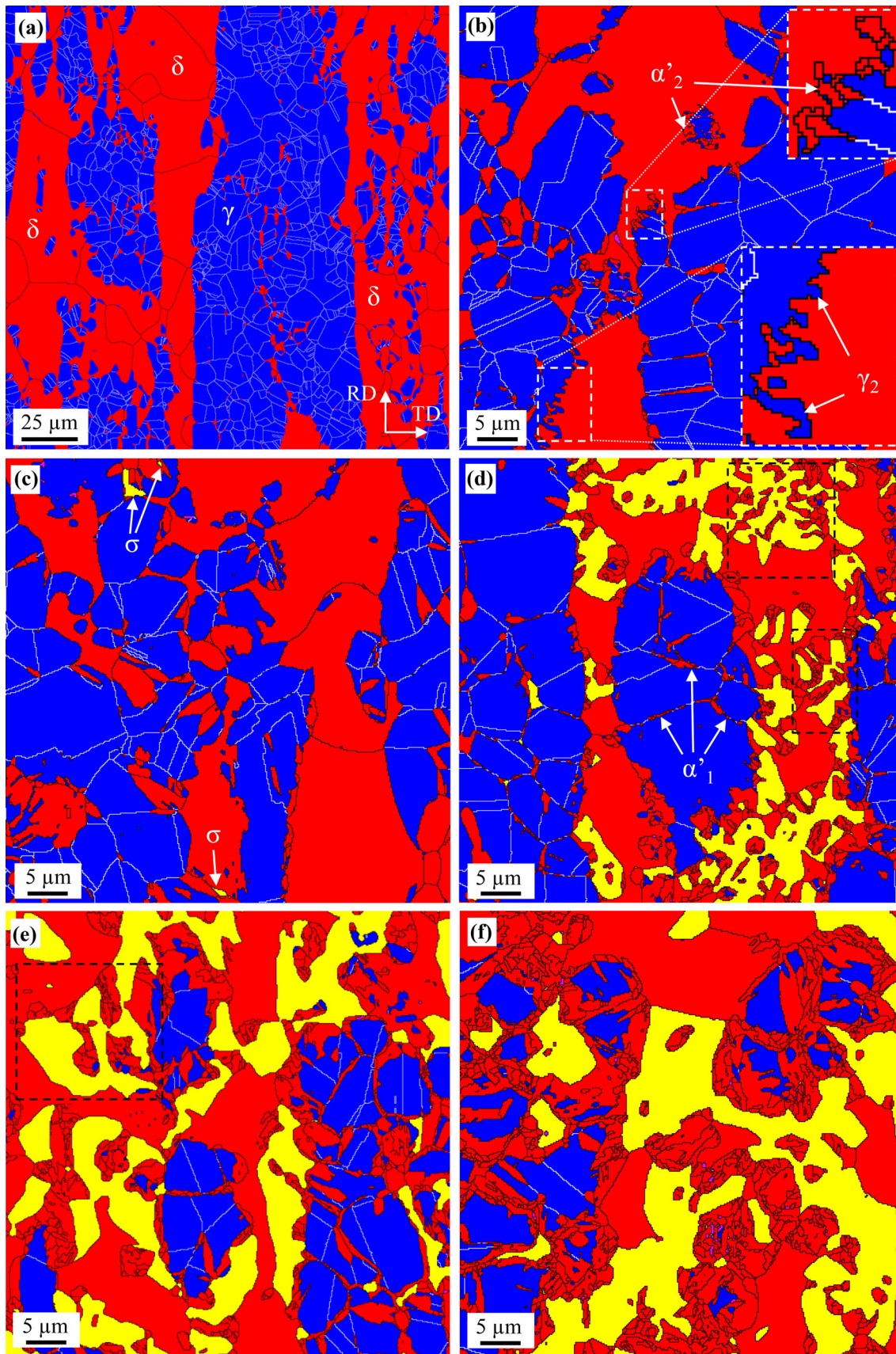


Fig. 1—EBSD phase maps of the normal section of the 2101 DSS sheet for various aging times at 963 K (690 °C): (a) as-received material before aging, (b) 10 h, (c) 24 h, (d) 120 h, (e) 350 h, and (f) 3300 h (δ -ferrite and bcc- α' -martensite in red, γ -austenite in blue, and σ phase in yellow; γ/γ grain boundaries are in white and δ/δ and δ/γ in black). The dotted boxes in (d) and (e) show that the σ phase and α'_2 are intertwined.

Table II. Chemical Composition of the γ and δ Phases Measured by Microprobe on the As-received 2101 DSS

	N	Ni	Cr	Mn	Si	Mo	Cu	V	Fe	C
γ	1.2 ± 0.4	1.7 ± 0.1	21.6 ± 0.3	5.3 ± 0.1	1.21 ± 0.03	0.14 ± 0.02	0.28 ± 0.06	0.08 ± 0.01	68.4 ± 0.3	0.17
δ	0.1 ± 0.2	1.16 ± 0.03	24.0 ± 0.2	4.7 ± 0.1	1.47 ± 0.01	0.20 ± 0.02	0.26 ± 0.03	0.09 ± 0.02	67.9 ± 0.2	0.035

The carbon content was estimated from Thermo-Calc calculations for the equilibrium stage at 1400 K (1123 °C) (atomic percent).

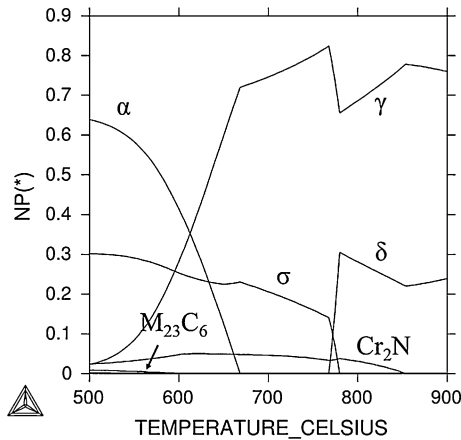


Fig. 2—Phase diagram of 2101 DSS calculated at equilibrium between 773 K and 1173 K (500 °C and 900 °C) using Thermo-Calc software (version S, database TCFE5). NP(*) represents the mole fraction of phases.

phases is equivalent^[13,32] and their composition is in good agreement with the experiment results. It is a slightly higher temperature than the assumed solution annealing temperature of 1323 K (1050 °C) because during the solution annealing the steel did not reach the thermodynamic equilibrium.^[32]

Figure 2 shows the equilibrium phase fractions of the investigated 2101 DSS, calculated using Thermo-Calc software between 773 K and 1173 K (500 °C and 900 °C). Precipitation and phase transformation are expected during aging at 963 K (690 °C). The volume fractions of precipitated phases predicted at equilibrium using Thermo-Calc calculations are 2.1 pct of Cr_2N nitrides, 0.3 pct of M_{23}C_6 carbides, and 23 pct of σ phase, whereas higher γ -austenite fraction (74.6 pct) and no δ -ferrite are expected.

B. Aging Kinetics at 963 K (690 °C)

The kinetics of the microstructural evolution of the as-received 2101 DSS during aging at 963 K (690 °C) was followed using both TPE and hardness measurements, as shown in Figure 3. The hardness curve is stable up to 32 to 64 hours of aging. In addition the TEP curve shows a complex microstructural evolution from a few minutes. Indeed, each inflection of the TEP curve can be attributed to a change of the dominant mechanism, as precipitation or a phase transformation. The TEP changes during aging are well above the maximum uncertainties of $0.02 \mu\text{V}\cdot\text{K}^{-1}$.

As observed in Figure 3, the first decrease of TEP occurs before 7 minutes of aging followed by an increase

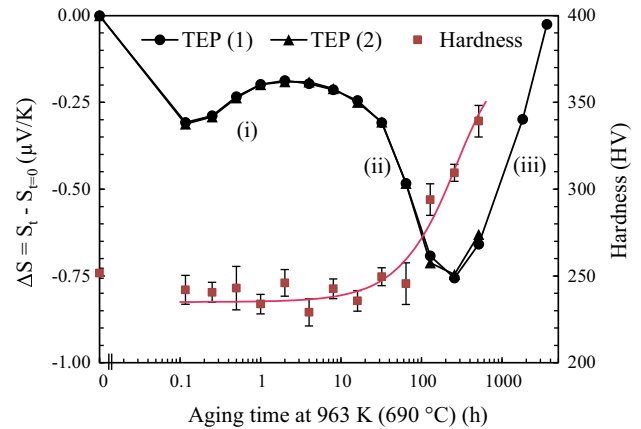


Fig. 3—Evolution of the TEP and hardness of the 2101 DSS during isothermal aging at 963 K (690 °C), measured at room temperature after water quenching.

of TEP from 7 minutes to 2 hours (i). Meanwhile, the hardness remains stable. As aging continues, the TEP drastically decreases between 16 and 128 hours (ii), while the hardness increases for aging times longer than 32 to 64 hours. The hardness response to this specific microstructural change appears delayed compared with the TEP measurements. This finding is observed most likely because the microstructural changes do not initially affect the hardness; the phenomenon must be well established to observe a modification of the hardness. Finally, for a relatively long aging time, more than 256 hours, the TEP increases sharply (iii). After 3600 hours of aging, the 2101 DSS did not reach thermodynamic equilibrium, as the TEP continues to increase. To characterize the microstructural changes responsible for the TEP evolution, different aging stages were selected for electron microscopy observations. A short aging of 15 minutes at 963 K (690 °C) was performed to investigate the early stages of precipitation. Isothermal heat treatments were performed at 963 K (690 °C) for 10, 24, and 120 hours to characterize the decrease of TEP (ii) and for 120, 350, and 3300 hours to understand the sharp increase of TEP (iii).

C. Evolution of Phases

The microstructural evolution of the 2101 DSS can be globally described by the EBSD maps in Figure 1. After 10 hours of aging, the phase boundaries are not as well-delimited and straight as those in the as-received sample (Figure 1(a)) but are more or less crumpled because γ grew in δ , as observed in Figure 1(b). This new

austenite has the same orientation as the primary γ with a different composition and a different morphology and is generally designated as γ_2 -secondary austenite.^[3,6,33] Some small grains of α' martensite, indexed as ferrite, are also observed along the γ/δ interfaces. This martensite originates from the partial transformation of the metastable γ_2 during the water quenching and is called α'_2 . Note that α'_2 is always in former δ grain, as γ_2 is the result of the growth of γ in δ during the aging.

The σ -phase precipitation is detected by EBSD after 24 hours of aging, as indicated in Figure 1(c), and was not observed in the 10-hours-aged sample, even by TEM. The σ -phase islands are present in δ at the γ/δ (or α'_2/δ) and δ/δ interfaces and are approximately 1- μm wide. The volume fraction of the σ phase measured after 24 hours of aging is approximately 0.1 pct. The OR between the matrix and σ was studied by EBSD. At the γ/δ interface, the σ phase is in OR1 with γ , known as Nanno OR,^[7] while at the δ/δ interface, the σ phase is in OR2 with one of the δ -grains, as indexed by Chen *et al.*^[7] on aged 2205 DSS for the initial stage of σ -phase precipitation in δ grains.

$$(001)_\sigma \parallel (111)_\gamma \quad \text{and} \quad [110]_\sigma \parallel [\bar{1}01]_\gamma \quad [\text{OR1}]$$

$$(\bar{3}\bar{1}\bar{2})_\sigma \parallel (211)_\delta \quad \text{and} \quad [\bar{1}\bar{1}\bar{2}]_\sigma \parallel [\bar{1}\bar{1}3]_\delta \quad [\text{OR2}]$$

As aging continues, the amount of σ and α'_2 increases, while the amount of δ decreases, as observed in Figure 4. The σ phase and α'_2 are clearly intertwined (see Figures 1(d) and (e)), and thereby, the σ phase and γ_2 appear to have grown in δ from γ/δ and δ/δ boundaries. In addition, after 120 hours of aging, islands of martensite are also observed at the γ/γ grain boundaries, see Figure 1(d). This martensite, transformed from the primary γ , is called α'_1 . As a fact, note that α'_1 is always in former γ grain.

The increase of the α'_1 volume fraction and the growth and coarsening of the σ phase in δ are clearly observed by EBSD in Figures 1(d) through (f) after 120, 350, and 3300 hours of aging, respectively. The σ -phase islands are indeed larger and less broken by α'_2 . These resulting two-phase transformations and the decrease of the γ fraction are directly observed in Figure 4. In addition, the decrease of the δ fraction is weaker after several hundred hours of aging. The microstructure of the 2101 DSS after 3300 hours of aging at 963 K (690 °C) followed by water quenching is globally composed of 17 pct γ , 15 pct δ , 23 pct σ , and 44 pct α' .

Figure 5(a) represents a close view on a former γ/δ phase boundary after 120 hours of aging followed by water quenching, as indicated by the dashed line. Some α'_2 are present in the former δ grain, as indicated by the white arrows. The corresponding stereographic projections show that the α'_2 laths and surrounding- γ grain are close to the K-S OR. Actually, the continuous pole figures observed are characteristics of the γ -fcc-to- α' -bcc transformation.^[30,34] It confirms that γ_2 is the parent phase of α'_2 , *via* the growth of γ in δ during aging.

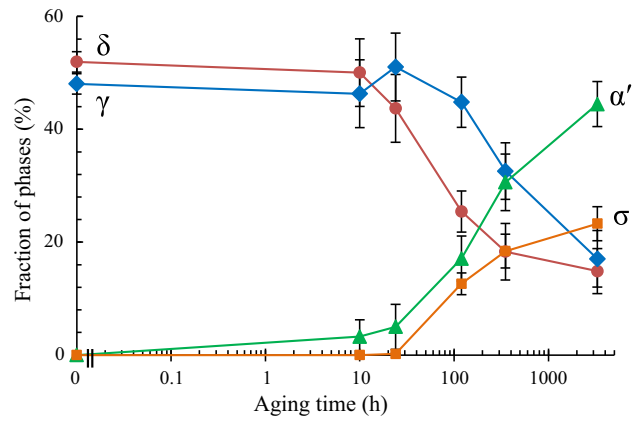


Fig. 4—Volume fractions of phases experimentally determined in the 2101 DSS according to aging time at 963 K (690 °C). The α' -martensite fraction is the addition of α'_1 and α'_2 .

Figure 5(b) shows a closer look on a former austenitic area after 3300 hours of aging. Some α'_1 laths are observed in the γ grains and along the γ/γ grain boundaries. The pole figures indicate that all the α'_1 laths in a single original γ grain present the K-S OR with this grain. As previously, it confirms that α'_1 originates from the transformation of the parent primary γ grain. Further investigations on air-cooled samples showed the same amount of α' and a similar TEP as for the water-quenched samples. Therefore, after aging, γ and γ_2 to α' transformations occur during cooling regardless of the cooling rate.

The chemical compositions in substitutional elements of the different phases are presented in Table III for the 3300-hours-aged state. Compared with the composition of δ in the as-received material presented in Table II, δ is depleted in Cr, Mn, Ni, and Mo, while the α'_2 issued from γ_2 is richer in Mn and Ni and the σ phase is richer in Cr, Mo, and Si, as expected as these elements are σ stabilizer.^[3] Other investigations on samples aged for 120 and 3300 hours reveal that the composition of the σ phase appears constant during aging. γ has the same composition in the as-received material and after 3300 hours of aging, while α'_1 is only depleted in Cr (looking at substitutional elements only).

D. Precipitation of Carbides and Nitrides

In the meantime, various types of precipitation are observed during aging at 963 K (690 °C). Starting at a few minutes of aging, Cr-rich precipitates nucleate and grow at grain boundaries. Examination of the replica of 2101 DSS aged for 15 minutes at low magnifications revealed that precipitates are located at γ/δ and δ/δ interfaces. TEM-SAD reveals that M_2N nitrides (simply designated as Cr_2N) and M_{23}C_6 are present at γ/δ interfaces, see Figure 7(a), whereas only Cr_2N are identified at δ/δ grain boundaries, and no precipitates are detected at γ/γ grain boundaries or intragranularly. TEM-energy dispersive X-ray spectroscopy (EDS), performed on the replicas, indicates that the M_{23}C_6

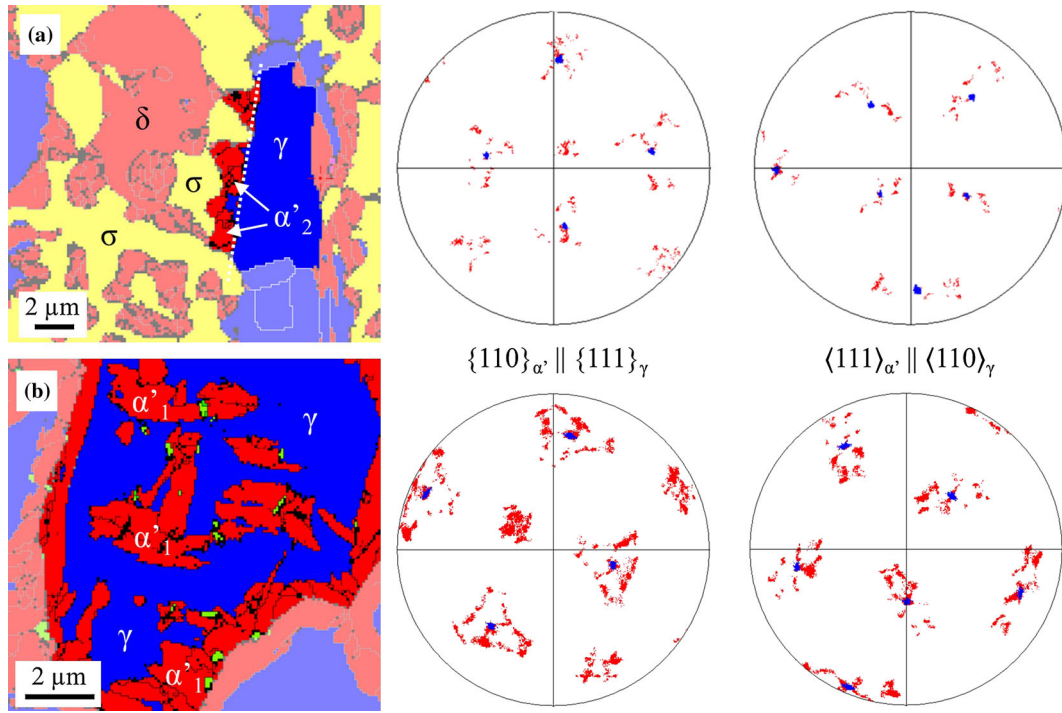


Fig. 5—EBSD phase maps showing the martensitic transformations in the 2101 DSS during aging at 963 K (690 °C): (a) γ_2 to α'_2 at a former γ/δ interface, as indicated by the white dashed line, after 120 h (γ in blue, α'_2 and δ in red, σ in yellow) and (b) γ_1 to α'_1 in γ at former γ/γ interfaces after 3300 h (γ in blue, α'_1 in red, Cr_2N in green). The superimposed pole figures of the α' -laths (red points) and the γ -parent grain (blue points) highlighted on each map are characteristic of the fcc-to-bcc transformation, represented here in K–S OR.^[30]

Table III. Chemical Composition of δ , γ , α'_1 , α'_2 , and σ Phase in 2101 DSS After 3300 h at 963 K (690 °C), Measured by EDS-TEM and EDS-SEM, in Atomic Percent

	Cr	Ni	Mn	Si	Mo	Fe
δ	20.9 ± 0.6	0.6 ± 0.1	3.4 ± 0.2	1.5 ± 0.1	0.06 ± 0.08	73 ± 1
γ	21.3 ± 0.7	1.7 ± 0.1	5.5 ± 0.3	1.3 ± 0.2	0.06 ± 0.07	68 ± 1
α'_1	19 ± 1	1.8 ± 0.2	5.6 ± 0.2	1.1 ± 0.2	0.07 ± 0.06	71 ± 2
α'_2	16.7 ± 0.6	2.1 ± 0.3	5.6 ± 0.4	1.5 ± 0.3	0.02 ± 0.04	73 ± 2
σ	33 ± 1	0.6 ± 0.2	5.0 ± 0.2	2.6 ± 0.2	0.6 ± 0.3	56 ± 1

carbides are mixed carbides ($\text{Cr}_{69}\text{Fe}_{25}\text{Mn}_6$) $_{23}\text{C}_6$ and that the Cr_2N nitrides are Cr rich with 2 to 3 at. pct of V, which is well known to increase the stability of M_2X nitrides.^[35]

At δ/δ grain boundaries, the Cr_2N have a rod-like morphology, 200 ± 100 nm long and 50 ± 20 nm wide, as observed in Figure 6(a). The precipitates are larger at triple points. During aging, the Cr_2N grow along the grain boundary to cover the entire interface, as observed in Figure 6(b). On the same grain boundary, most of the Cr_2N have the same orientation, in OR3 with one of the δ grains.

$$(0001)_{\text{Cr}_2\text{N}} \parallel (110)_{\delta} \quad \text{and} \quad [\bar{1}100]_{\text{Cr}_2\text{N}} \parallel [\bar{1}11]_{\delta} \quad [\text{OR3}]$$

At γ/δ phase boundaries, the Cr_2N have the same rod-like morphology as at δ/δ interfaces, whereas the

M_{23}C_6 have a particular triangular morphology, with an equivalent diameter of 130 ± 60 nm (see Figure 7(a)). A similar M_{23}C_6 morphology was observed by Hong *et al.*^[36] at γ/γ grain boundaries in austenitic stainless steel. At the phase boundaries, the Cr_2N are in OR3 with δ or in OR4 with γ . However, as the analyzed γ/δ interfaces do not systematically exhibit K–S or N–W OR, Cr_2N do not exhibit OR3 and OR4 simultaneously, as in the studies performed by Lee *et al.*^[33] and Ramirez *et al.*^[8]

$$(0001)_{\text{Cr}_2\text{N}} \parallel (111)_{\gamma} \quad \text{and} \quad [\bar{1}100]_{\text{Cr}_2\text{N}} \parallel [\bar{1}10]_{\gamma} \quad [\text{OR4}]$$

The M_{23}C_6 are in cube-on-cube OR5 with γ (see Figure 7(c)), and no particular OR was detected with δ . OR5 is common in austenitic stainless steel and has also

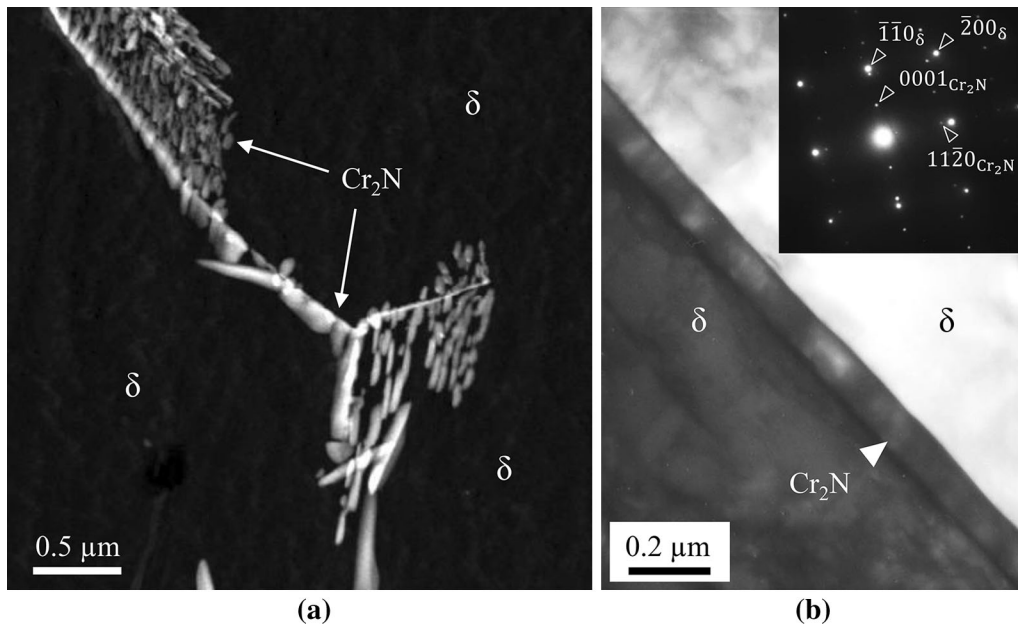


Fig. 6—Microstructure of aged 2101 DSS at 963 K (690 °C) along δ/δ phase boundary: (a) TEM-HAADF micrograph of Cr_2N on carbon replica prepared from sample aged for 15 min; (b) BF-TEM image of thin foil prepared from sample aged for 120 h and the corresponding SADP ($z = [1\bar{1}00]_{\text{Cr}_2\text{N}} \parallel [001]_{\delta}$).

been observed in 2205 DSS by Lee *et al.*^[6] and Chen *et al.*^[7]

$$(001)_{\text{M}_{23}\text{C}_6} \parallel (001)_{\gamma} \text{ and } [001]_{\text{M}_{23}\text{C}_6} \parallel [001]_{\gamma} \quad [\text{OR5}]$$

From 15 minutes of aging, the precipitates and γ_2 grow simultaneously, as observed in Figure 7(b). Unlike the γ/δ and δ/δ interfaces, no precipitation occurs during the first stage of aging at γ/γ interfaces. Nevertheless, after several hours of aging, a low density of Cr_2N is detected at the γ/γ interfaces, mainly along twins and at triple points. After 3300 hours of aging, intragranular Cr-rich precipitates were also observed in γ by SEM and indexed as Cr_2N by EBSD, as observed in Figure 8. The intergranular Cr_2N at the γ/γ grain boundary are indicated by the green arrows in the same figure.

The intragranular Cr_2N precipitate in particular directions, as observed in the BSE image of Figure 8(a). Precise OR4 is indexed by EBSD for Cr_2N strictly surrounded by γ . However, the Cr_2N nitrides surrounded by α'_1 are slightly disoriented from OR4 with γ but are in precise OR3 with α'_1 . This process most likely occurs during cooling because of the γ to α'_1 transformation. Along initial γ/γ grain boundaries, the same ORs were observed between intergranular Cr_2N and one of the γ grains or with α'_1 . The Cr_2N nitrides observed along γ -twin boundaries are in precise OR2 with the twin boundary.

The size distribution and fraction of the precipitates were quantified using BSE-SEM as a function of the aging time. Using BSE-SEM, no difference of chemical contrast was observed between M_{23}C_6 and Cr_2N .

However, looking at the morphology, the growth of the rod-like Cr_2N with aging time is clearly observed using SEM, and indexed using EBSD, *e.g.*, after 3300 hours in the γ (see Figure 8). Meanwhile, the M_{23}C_6 appear to be of constant size after 15 minutes of aging, as revealed by TEM observations. For example, the measured mean diameters after 15 minutes and 10 hours are equivalent (see Figures 7(a) and (c)). Therefore, the increase of the precipitate size and fraction, represented in Figures 9 and 10, respectively, is assumed to be the growth of the Cr_2N nitrides only.

From 15 minutes to 3300 hours of aging, the mean diameter of the precipitates increases linearly with the logarithm of aging time, as observed in Figure 9(a). Figure 9(b) shows that the distributions of the diameter are wider with aging time. During the first stages of aging, the number of nitrides is high with homogeneous size, and as aging continues, the density of precipitates decreases due to coarsening, growth, and dissolution in other phases. Figure 10 shows the evolution of the precipitate volume fraction, which is mainly attributed to the Cr_2N fraction as explained previously, which increases globally in two steps. The first step, at approximately 0.7 pct after 2 hours of aging, corresponds to the growth of Cr_2N at δ/δ interfaces and to the growth of precipitates at γ/δ interfaces. Between 2 and 350 hours of aging, a plateau is observed, most likely because the growth of Cr_2N is compensated by its absorption by the σ phase, mainly along δ/δ interfaces. After this time, SEM observations indicate that almost all of the Cr_2N at δ/δ interfaces have been dissolved. The second step is due to the Cr_2N growth at γ/δ interfaces and the precipitation of intragranular Cr_2N in austenite.

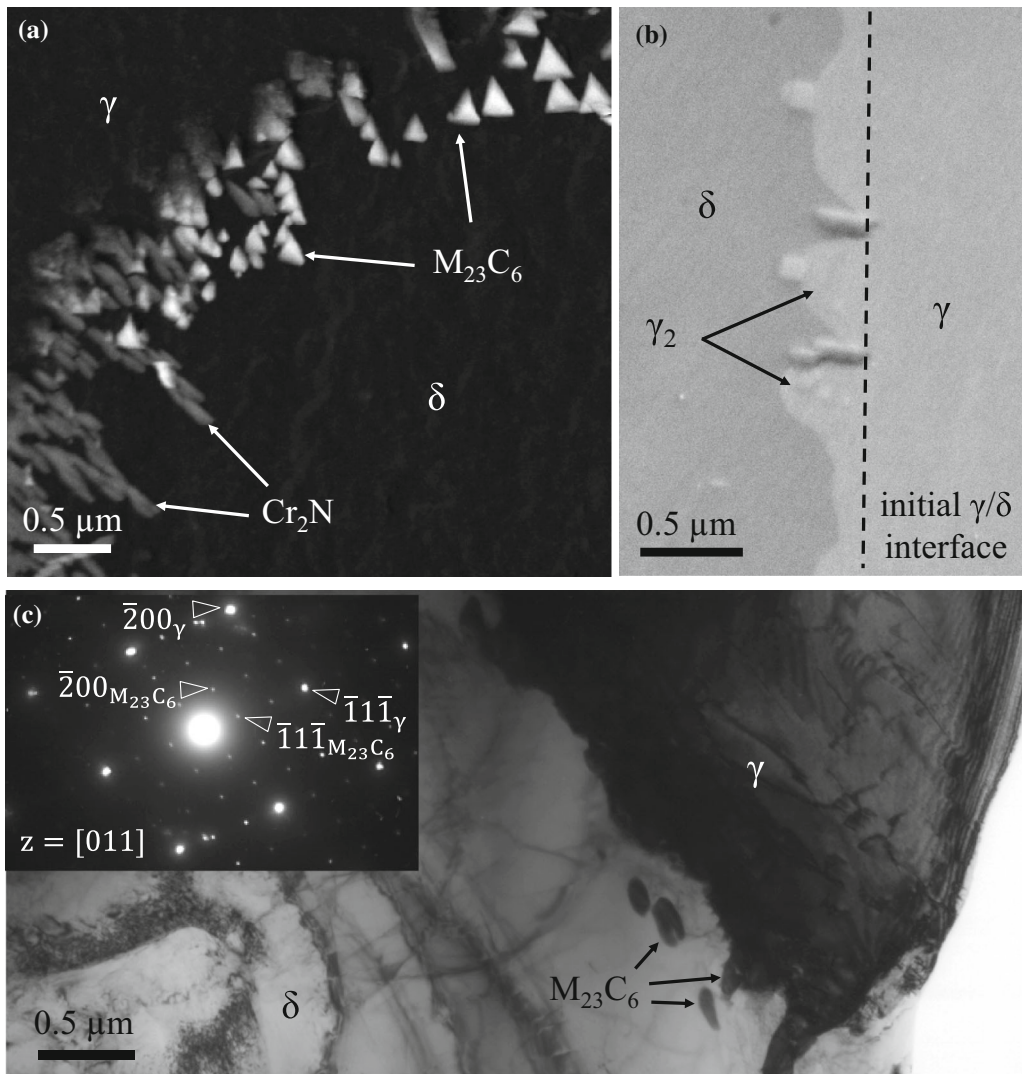


Fig. 7—Microstructure of aged 2101 DSS at 963 K (690 °C) along γ/δ phase boundary: (a) TEM-HAADF micrograph of Cr_2N and M_{23}C_6 precipitates on carbon replica prepared from sample aged for 15 min; (b) SE-SEM image showing precipitates and γ_2 growing in δ after 15 min of aging; (c) TEM-BF and SADP of intergranular M_{23}C_6 in cube-on-cube OR with the γ -grain, observed on a thin foil sample aged for 10 h.

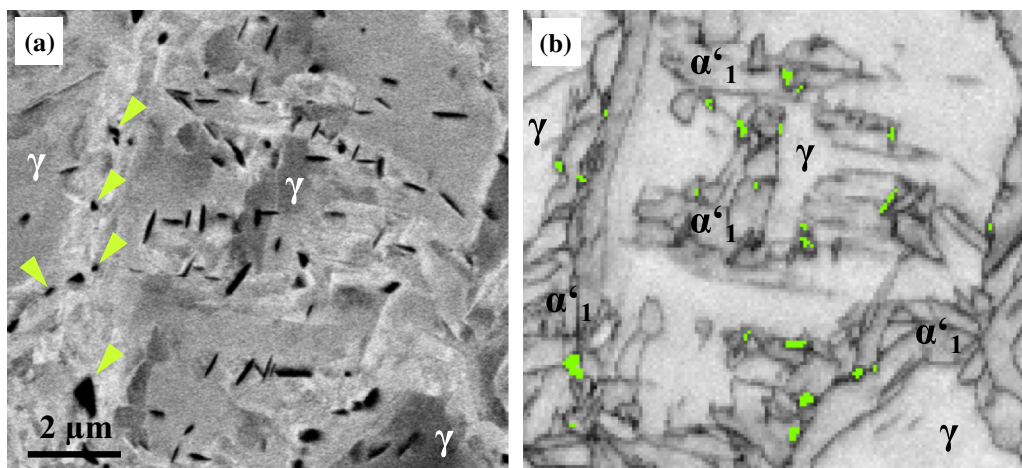


Fig. 8—(a) BSE-SEM image and (b) EBSD band contrast map (with indexed Cr_2N in green) of γ -grains in 2101 DSS aged for 3300 h, corresponding to the EBSD phase map of Fig. 5(b). In the BSE image, the Cr_2N along the original γ/γ interfaces and the intragranular Cr_2N appear in dark contrast, and in the EBSD band contrast map, the α'_1 -martensite laths are apparent.

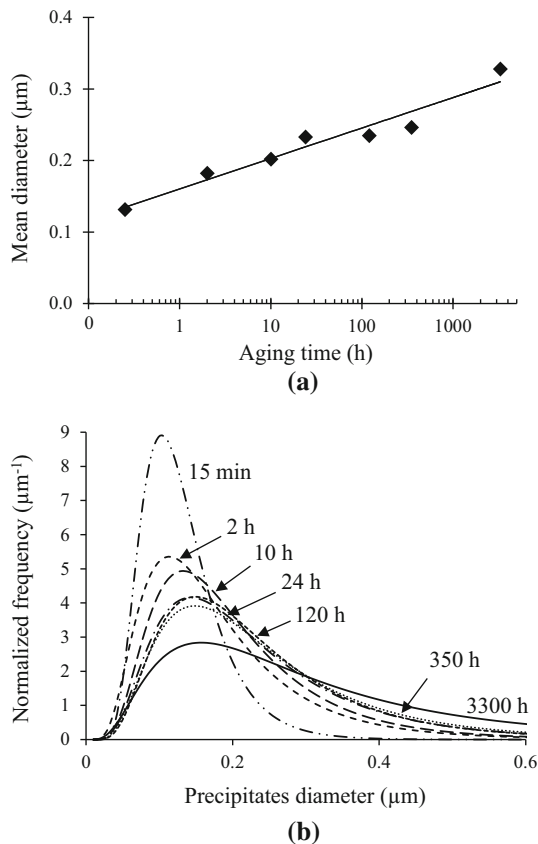


Fig. 9—(a) Evolution of the mean diameter of the precipitates in the 2101 DSS as a function of aging time at 963 K (690 °C) and (b) corresponding precipitate size distributions determined experimentally and fitted by log-normal laws.

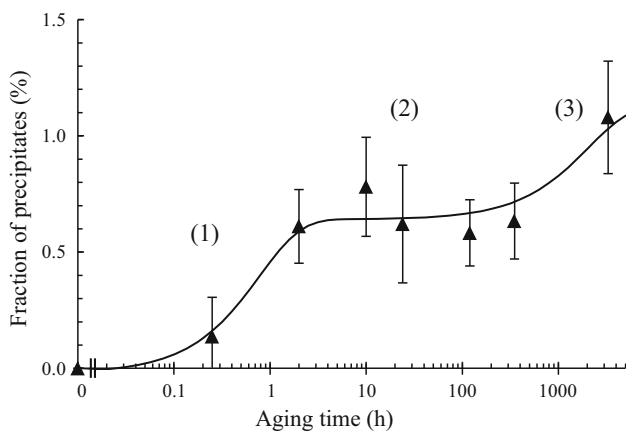


Fig. 10—Volume fraction of precipitates, which is mainly attributed to the Cr₂N fraction, in the 2101 DSS as a function of aging time at 963 K (690 °C), fitted with a double sigmoid.

IV. DISCUSSION

In this section, the mechanisms governing the microstructural changes previously presented are discussed. Based on the detailed characterization, we will describe the precipitation and phase transformations occurring during aging at 963 K (690 °C). For the

martensite originating from γ transformation during cooling, we consider that the α'_1 and α'_2 experimentally observed at room temperature are the Cr-depleted primary γ ($\gamma_{\text{-Cr}}$) and γ_2 , respectively, at 963 K (690 °C). Note that lower Cr, N, and C contents result in a decrease of γ stability due to an increase of its Ms temperature.^[37] Depending on the depletion of alloying elements, γ can partially or completely transform into martensite during cooling.

At 963 K (690 °C), the mechanisms of precipitation and phase transformation are diffusion dependent. We will use the diffusion kinetics of the alloying elements described in the literature and the estimated solubility of the interstitial elements N and C to support our analysis. The orders of magnitude of the radial diffusion distances for Cr, Ni, N, and C according to aging time are presented in Figure 11. The kinetics of diffusion of all the substitutional elements is assumed to be of the same order of magnitude,^[38] and with the kinetics of diffusion in pure iron and stainless steels being very similar,^[39] the chemical diffusion coefficients were acquired from data for pure iron.^[38] Diffusion is faster in bcc-ferrite than in fcc-austenite because of the higher density of the fcc-structure. Starting at a few minutes of aging, interstitial elements can diffuse in the entire grains for both γ and δ phases. Thus, the diffusion of C and N can be considered infinite, and their concentrations can be considered homogeneous in each phase. The diffusion of substitutional elements is much more sluggish, and radial diffusion reaches the grain size after approximately 100 hours in δ and 10000 hours in γ . On the other hand, the solubility limits of N and C in γ of the studied 2101 DSS were calculated at 963 K (690 °C) with Thermo-Calc software: $[\text{C}]_{\gamma} = 0.02$ at. pct and $[\text{N}]_{\gamma} = 0.12$ at. pct. In δ , the solubility is commonly assumed to be ten times lower and may be assumed to be zero. The solubility at 963 K (690 °C) is thus low compared with the amount of N and C in the as-received material (see Tables I and II). The excess of N and C tends to precipitate.

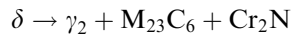
The mechanisms of microstructural evolution during non-interrupted aging at 963 K (690 °C) are first discussed separately at γ/δ , δ/δ , and γ/γ interfaces. Then, the evolution of the microstructure after water quenching is described as a whole, and the interaction of all the mechanisms is discussed.

A. Microstructural Mechanisms at γ/δ Interfaces

The evolution of the microstructure at γ/δ interfaces is schematically represented in Figure 12. The fast nucleation of Cr₂N and M₂₃C₆ at phase boundaries is due to the high coherency between the crystal lattices of the precipitates and the crystal lattices of the matrix phases, δ or γ . Indeed, OR3, OR4, and OR5 between the precipitates and the matrix phase are characterized by parallel close-packed planes and directions, resulting in a low interfacial energy.

The nucleation of Cr₂N and Cr-rich M₂₃C₆ attracts substitutional elements, mainly Cr, from short-path diffusion. At the vicinity of the γ/δ phase boundary, the Cr depletion is located first in δ because Cr diffusion is

faster in δ than in γ . As Cr is a ferrite stabilizer, the δ depleted transforms into γ_2 due to the growth of γ in δ . Thus, a cooperative growth of the precipitates and of γ_2 is observed, and the δ transformation at the γ/δ interface is globally described as



The newly formed γ_2 is poorer in Cr than the primary γ . The C and N contents in the material are also globally lower, consumed by precipitation.

From Figure 11, the expected width of the Cr-depleted δ is 0.1 to 0.2 μm after 15 minutes of aging, which is consistent with the width of γ_2 shown in Figure 7(b). This result confirms that the diffusion of Cr in δ is the limiting factor of the δ transformation. In Figure 12, the migration of the γ/δ interface is schematically presented in b and c, pinned on precipitates. No discontinuous or lamellar precipitation has been observed between the precipitates and the matrix, as sometimes reported for

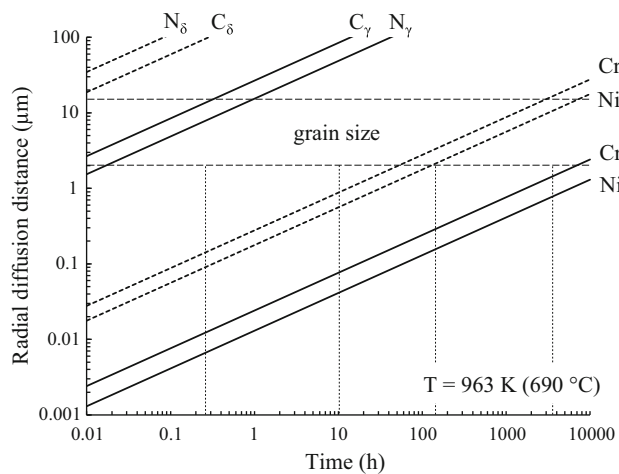
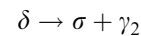


Fig. 11—Average radial diffusion distance of different alloying elements during aging at 963 K (690 °C) in γ and δ . The chemical diffusion coefficients were obtained from “Diffusion in Solids Metals and Alloys”.^[38]

DSS in the literature.^[6] Cr_2N grow along the interface in δ , whereas $M_{23}C_6$ stop growing after as little as 15 minutes of aging, most likely because no additional supersaturated C remains in the solid solution due to the low carbon content in the as-received material.

At the γ_2/δ interface, it is possible that the excess of α stabilizing elements in γ_2 , such as Cr and Mo, diffuses into the adjacent δ , while the excess of Ni in δ is absorbed by γ_2 . Because α stabilizers are globally σ stabilizers, the σ phase precipitates in δ once the N, C, and Ni contents in δ are low enough, as these elements prevent the precipitation of the σ phase.^[26,40,41] In the investigated 2101 DSS, this precipitation occurs between 10 and 24 hours of aging at 963 K (690 °C). The σ phase nucleates in OR1 with γ , for which the crystallographic coherency is better than with δ . The σ phase grows in δ because of the higher Cr and Mo contents and the higher diffusivity of substitutional elements in δ than in γ . This process occurs by a second transformation of the δ -ferrite (see Figure 12(e)):



During the migration of the phase boundary, Cr, Mo, and Si are absorbed by the σ phase, while Ni is rejected to γ_2 . This transformation is known to occur in higher-alloyed DSS, and some authors refer to an eutectoid decomposition of δ .^[3,5,6,33] Mn does not appear to affect the nucleation and growth of the σ phase as the Mn content in the σ phase is only slightly higher than in δ for the as-received material. As the Cr content in the σ phase is high, γ_2 becomes increasingly depleted in Cr with aging time. The chemical measurements presented in Table III also reveal the long-range Mn and Ni diffusion from δ to γ_2 and the Cr diffusion from δ to σ phase. Therefore, the chemical driving force of the δ -transformation decreases until it stops. This is experimentally observed for aging times longer than 100 hours, with a volume fraction of γ_2 that is no longer increasing (considering $fv_{\gamma_2}(t) = fv_{\delta}(t_0) - fv_{\delta}(t) - fv_{\sigma}(t)$ as the σ phase grows only in δ , values of 14, 15, and 14 pct for $fv_{\gamma_2}(t)$ are calculated for $t = 120, 350,$ and

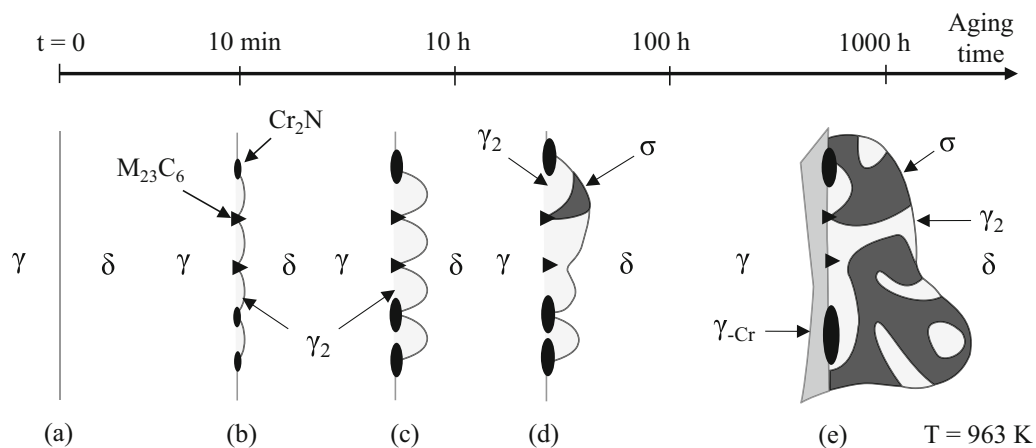


Fig. 12—A schematic illustration of the microstructural evolution of 2101 DSS during aging at 963 K (690 °C) at γ -austenite/ δ -ferrite interfaces (γ -Cr represents the Cr-depleted primary γ).

3300 hours of aging, respectively, from the data presented in Figure 4).

An increase of the σ -phase volume fraction and changes of the σ -phase and γ_2 morphologies are nevertheless observed for longer aging times because of the coarsening and growth of σ -phase islands. This mechanism is associated with the Cr depletion of the primary γ , which is fully described in Section IV-C.

B. Microstructural Mechanisms at δ/δ Interfaces

A schematic representation of the microstructural evolution at δ/δ boundaries is presented in Figure 13. Similar to γ/δ interfaces, the fast nucleation of Cr_2N is due to the high coherency between Cr_2N and δ . With N diffusion being fast in the iron matrix, Cr limits the kinetics of precipitation and is absorbed from short-path diffusion during Cr_2N growth, leading to Cr-depleted δ at the vicinity of grain boundaries. However, no γ_2 formation is observed along δ/δ interfaces, and there is no δ transformation, as observed at δ/γ interfaces. The interfacial energy required for γ_2 nucleation is most likely too high.

The precipitation of the σ phase is observed after 24 hours of aging at the δ/δ grain boundary. The N content is low in δ , and the amount of Cr available is larger at δ/δ than at δ/γ interfaces. A likely scenario is that supersaturated N in δ is completely consumed by Cr_2N precipitation, and N becomes the limiting factor in the Cr_2N growth. The Cr contents in δ would again be homogeneous, and the N content is very low, allowing the σ phase to nucleate at $\delta/\text{Cr}_2\text{N}$ interfaces in OR5 with δ .

The σ phase grows along δ/δ interfaces, where the diffusion is faster, and expands into the two adjacent δ -grains, absorbing Cr from the surrounding δ and absorbing Cr_2N . The dissolution of trapped Cr_2N provides an excess of N, leading to the γ_2 nucleation. Based on the experimental results, a similar reaction to the second δ transformation at δ/γ interfaces is proposed:

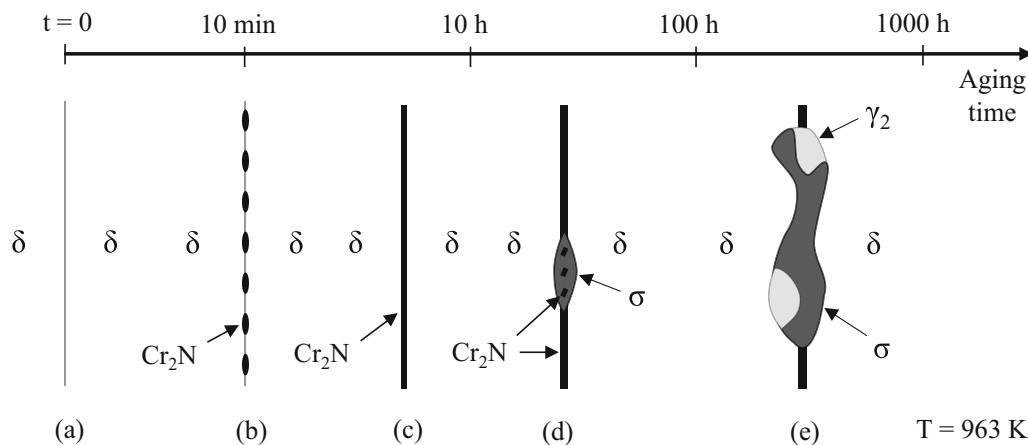
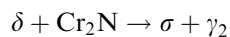


Fig. 13—A schematic illustration of the microstructural evolution of 2101 DSS during aging at 963 K (690 °C) between two δ -ferrite grains.

The diffusion mechanisms are similar to those explained in Section IV-A, and the sequence is summarized in Figures 13(c) through (e). Villanueva *et al.*^[5] demonstrated that the kinetics of σ -phase precipitation is faster in DSS than in ferritic stainless steels because the presence of austenite promotes σ -phase precipitation through a eutectoid transformation facilitated by the growth of austenite. Considering this point and the EBSD maps obtained in this study, it appears that in 2101 DSS, the σ phase nucleates preferentially at γ/δ interfaces and then propagates along δ/δ grain boundaries following the δ transformation above, where a large amount of Cr and N is provided by Cr_2N dissolution.

C. Microstructural Mechanisms at γ/γ Interfaces and in γ

Cr_2N nitrides are observed at γ/γ grain boundaries after 10 hours of aging at 963 K (690 °C). Although the crystallographic coherency is high between Cr_2N and γ , precipitation is more sluggish than at γ/δ and δ/δ interfaces. Indeed, diffusion in austenite is more than 100 times slower than in ferrite. The radial diffusion distance of Cr in γ after 10 hours at 963 K (690 °C), estimated from Figure 11, is approximately 50 nm. This result is consistent with the length of Cr diffusion in δ corresponding to the early stages of precipitation observed at γ/δ and δ/δ after a few minutes of aging (see Figure 11).

At γ/γ interfaces, Cr_2N nitrides are first observed at triple points, then on classic grain boundaries, and then on twin boundaries, in good agreement with the increasingly lower interfacial energies of these three nucleation sites. Finally, intragranular precipitation in γ occurs after more than 1000 hours of aging as the nucleation energy required is high. A schematic representation of the sequence of microstructural evolution is presented in Figure 14. No M_{23}C_6 carbides were detected at γ/γ interfaces, which supports the hypothesis that no additional C is available in the material due to its consumption by M_{23}C_6 precipitation at γ/δ phase boundaries.

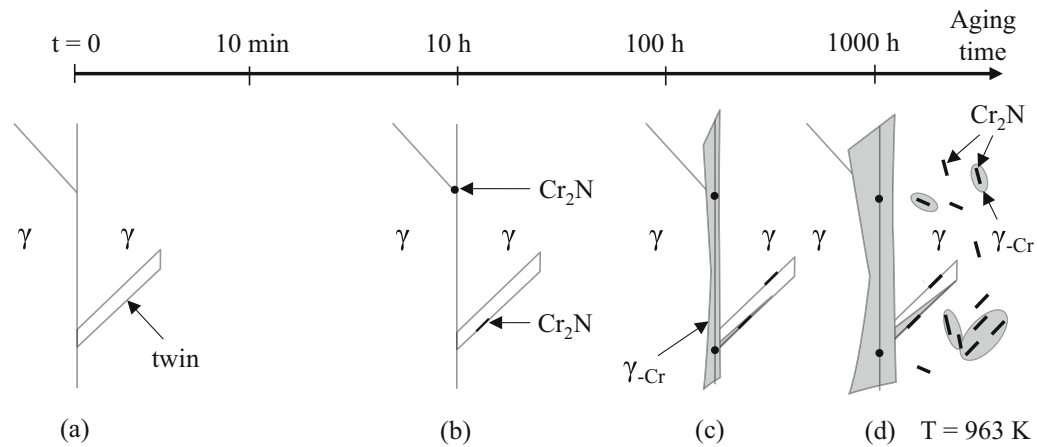


Fig. 14—A schematic illustration of the microstructural evolution of 2101 DSS during aging at 963 K (690 °C) between two austenite grains (γ -Cr represents the Cr-depleted primary γ).

After 100 hours of aging at 963 K (690 °C), the primary γ is locally Cr depleted along γ/γ grain boundaries and around the intragranular Cr_2N (see Figure 5(b)). The N and C contents are also globally lower in γ due to precipitation at all the interfaces. The Cr-depleted primary γ is metastable and transforms into α'_1 martensite during cooling.

At γ/γ boundaries, two mechanisms lead to the depletion of Cr: the precipitation of Cr_2N and, probably the most important mechanism, the growth and coarsening of the σ phase in δ . Indeed, after 3300 hours of aging, a large volume fraction of γ is Cr depleted, whereas the Cr_2N fraction at γ/γ interfaces is weak. In addition, the Cr depletion of the primary γ occurs mainly during the growth and coarsening of the σ phase after more than 100 hours of aging. With the fraction of γ_2 being constant, a significant amount of Cr is required for σ -phase growth and coarsening and is provided by the primary γ .

The growth of the σ phase in δ attracts Cr from long-path diffusion along γ grain boundaries, as intergranular diffusion is much faster than volume diffusion.^[42] The time required for Cr diffusion along γ/γ boundaries may be neglected compared with the time required for the volume diffusion of Cr in γ to reach the grain boundary. Using SEM-EDS maps, the width of this Cr-depleted γ zone was estimated to be approximately 0.5 μm after 120 hours of aging, and the width of γ transformed in α'_1 along γ/γ interfaces after 3300 hours of aging is approximately 2 μm , as estimated from EBSD maps (see Figure 1(f)). These results are in good agreement with the radial diffusion distance of Cr in γ presented in Figure 11. This result confirms that the amount of primary γ transformed in α'_1 during cooling is limited by the Cr diffusion during aging at 963 K (690 °C).

D. Aging of 2101 DSS: A Global Perspective

The mechanisms that govern the microstructural evolution of 2101 DSS during aging at 963 K (690 °C)

were described separately for the three interfaces. However, these mechanisms are not independent and are jointly discussed in this section. The microstructural evolutions will be presented after quenching at room temperature as will their respective effects on the TEP. For this purpose, the curves of the measured phase fractions presented in Figures 4 and 10, the TEP curve presented in Figure 3, and all the microstructural evolutions summarized in Figure 15 are compared.

The precipitation of Cr_2N at γ/δ and δ/δ interfaces and of M_{23}C_6 at γ/δ interfaces is observed after a few minutes of aging at 963 K (690 °C). The increase of the precipitate fraction (1) in Figure 10 after a few minutes up to 2 hours of aging is in good agreement with the increase of TEP (i) observed in Figure 3. Indeed, N and C in solid solution have a negative effect on the TEP of iron.^[21–23] The precipitation of Cr_2N and M_{23}C_6 decreases the amount of N and C in solid solution, leading to an increase of the TEP of the material. This effect was also reported by Caballero *et al.*^[43] for M_{23}C_6 in martensitic stainless steel.

The growth of precipitates is accompanied by a transformation of δ in γ_2 at γ/δ interfaces, resulting in Cr depletion due to Cr_2N and M_{23}C_6 precipitation (see Figures 15(b) and (c)). The growth of M_{23}C_6 nevertheless stops after less than 1 hour of aging. As γ_2 is less alloyed than the primary γ , especially in Cr, γ_2 is metastable and partially transforms into α'_2 martensite during cooling. After approximately 10 hours of aging, a low density of Cr_2N is also observed at γ/γ interfaces, which is consistent with the kinetics of Cr diffusion in γ .

For aging times between 10 and 24 hours, the σ phase nucleates at γ/δ and δ/δ interfaces and grows through a second transformation of δ in the σ phase and γ_2 . This transformation occurs mainly at γ/δ phase boundaries and is promoted along δ/δ grain boundaries by the absorption of Cr_2N , which provides Cr and N for the σ phase and γ_2 , respectively (see Figures 15(d) and (e)). The dissolution of Cr_2N most likely causes the plateau observed in the curve of the precipitate fraction (Figure 10(2)). This second δ transformation is

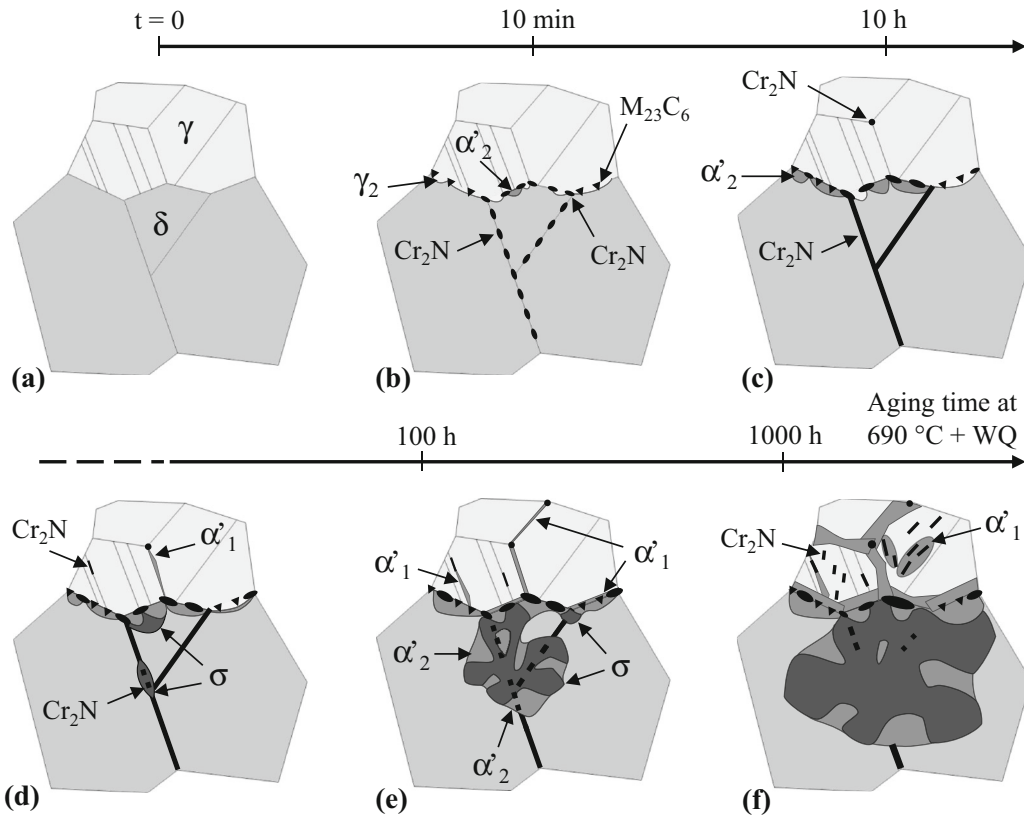


Fig. 15—A schematic illustration of the global microstructural evolution of 2101 DSS observed at room temperature after aging at 963 K (690 °C) followed by water quenching.

accurately followed in the TEP evolution, which decreases drastically from 16 to 250 hours (zone (ii) in Figure 3). In this range of aging times, the effect of this transformation on the TEP is predominant on the effects of the other mechanisms, such as the growth of the precipitates. The decrease of TEP caused by σ -phase precipitation was also reported by Lara *et al.*^[44] during aging of a 2205 DSS. Thereafter the δ transformation stops before all the δ ferrite is consumed, contrary to what is observed during aging of 2205^[5] and 2507^[3] DSS.

The increase of the Cr_2N fraction (3) in Figure 10 is due to the growth and coarsening of Cr_2N at γ/δ and γ/γ interfaces and to the precipitation of intragranular Cr_2N in γ , which, in combination with the growth and coarsening of the σ phase, leads to a gradual depletion of the primary γ . The primary γ transforms into α'_1 at γ/δ phase boundaries, at γ/γ grain boundaries, and around intragranular Cr_2N from 100 hours up to 3600 hours of aging, as represented in Figures 15(e) and (f). The decrease of the γ fraction and the increase of the α' fraction in Figure 4 are correlated with the sharp increase of the TEP (iii) in Figure 3. For this range of aging times, the effect of this martensitic transformation is more important than the effect of the growth and coarsening of the σ phase on the TEP. The second increase of the precipitate fraction may also contribute to the increase of TEP; however, its effect should be much lower than the martensitic transformation,

considering the increase of TEP (i) and (iii) and the large amount of γ transformed into α'_1 after cooling from 250 to 3300 hours of aging. The positive effect of the γ -to- α' transformation on the TEP contradicts the results of Caballero *et al.*,^[43] which indicated that the presence of γ at the expense of α' increases the TEP in a stainless steel.

After 3300 hours of aging at 963 K (690 °C), the trend of the TEP curve indicates that the 2101 DSS did not reach equilibrium. Furthermore, the large proportion of remaining δ -ferrite is far from calculated equilibrium using the Thermo-Calc software (see Figure 2). For longer aging times, the expected microstructural changes are the growth and coarsening of the σ phase and Cr_2N combined with Cr depletion of all the primary γ after approximately 10,000 hours in view of Figure 11. After cooling, the primary γ will be completely transformed into α'_1 martensite.

V. CONCLUSIONS

The complementary nature of the analysis techniques used provides an accurate understanding of the microstructural evolution of 2101 DSS during long-term aging in the embrittlement nose temperature range. TEP measurements were used as a tool to identify the time at which modifications in the microstructure occurs and to select specific aging time. A multi-scale electron

characterization at given time, allows a clear and quantitative description of the mechanisms of precipitation and phase transformation occurring. The complex evolution of the microstructure was understood with the coupling of those two methods. All the microstructural evolution mechanisms occurring during aging are mainly controlled by chromium diffusion.

1. Rapid precipitation of Cr₂N and M₂₃C₆ occurs after only a few minutes of aging. At the γ/δ phase boundary, δ -ferrite transforms following $\delta \rightarrow \gamma_2 + M_{23}C_6 + Cr_2N$, whereas at the δ/δ grain boundary, only Cr₂N precipitate. Precipitation is more sluggish at the γ/γ grain boundary, where Cr₂N were observed later after 10 hours of aging.
2. M₂₃C₆ have a triangular morphology and stop growing after a relatively short aging time, unlike Cr₂N, which have a rod-like morphology and grow continuously. The fraction and density of Cr₂N are much higher than that of M₂₃C₆.
3. The local composition changes due to the precipitation lead to σ -phase nucleation at both γ/δ and δ/δ interfaces after 24 hours of aging; the σ phase grows through the transformation $\delta \rightarrow \gamma_2 + \sigma$. Compared with classic DSS, the increase of the N content and the decrease of the Cr and Mo contents in 2101 lean duplex are not sufficient to avoid σ -phase precipitation; however, its nucleation is considerably retarded and the δ transformation stops before the complete consumption of the δ ferrite.
4. Both the γ_2 formed during the δ transformations and for longer aging times the primary γ , depleted in chromium by Cr₂N and the σ -phase growth, are metastable and transform into martensite during cooling. 2101 DSS is thus sensitive to martensitic transformation after aging.
5. After 3300 hours of aging, the 2101 DSS is still not at equilibrium, with 15 pct δ , 23 pct σ phase, 17 pct γ , and 44 pct martensite after cooling.

ACKNOWLEDGMENTS

We would like to thank the CLYM (Centre Lyonnais de Microscopie <http://www.clym.fr>) for access to the JEOL 2010F microscope. The author would also like to express his gratitude to Professor C. Esnouf and Professor C. Hutchinson for their fruitful discussions.

REFERENCES

1. J. Charles and P. Chemelle: *8th Duplex Stainless Steels Conference*, Beaune, 2010, p. 29.
2. I. Alvarez-Armas and S. Degallais-Moreuil: *Duplex Stainless Steels*, ISTE & Wiley, New York, 2009.
3. J.O. Nilsson: *Mater. Sci. Technol.*, 1992, vol. 8, pp. 685–700.
4. T.H. Chen, K.L. Weng, and J.R. Yang: *Mater. Sci. Eng. A*, 2002, vol. 338, pp. 259–70.
5. D.M.E. Villanueva, F.C.P. Junior, R.L. Plaut, and A.F. Padilha: *Mater. Sci. Technol.*, 2006, vol. 22, pp. 1098–104.
6. K.M. Lee, H.S. Cho, and D.C. Choi: *J. Alloy Compd.*, 1999, vol. 285, pp. 156–61.
7. T.H. Chen and J.R. Yang: *Mater. Sci. Eng. A*, 2001, vol. 311, pp. 28–41.
8. A.J. Ramirez, J.C. Lippold, and S.D. Brandi: *Metall. Mater. Trans. A*, 2003, vol. 34A, pp. 1575–97.
9. C.M. Garzon and A.J. Ramirez: *Acta Mater.*, 2006, vol. 54, pp. 3321–31.
10. P. Johansson and M. Liljas: *4th European Stainless Steel Science and Market Congress*, Paris, 2002, p. 153.
11. E. Alfonsson: *8th Duplex Stainless Steels Conference*, Beaune, 2010, p. 787.
12. W. Zhang, L.Z. Jiang, J.C. Hu, and H.M. Song: *Mater. Charact.*, 2009, vol. 60, pp. 50–55.
13. M. Liliyas, P. Johansson, H.P. Liu, and C.O.A. Olsson: *Steel Res. Int.*, 2008, vol. 79, pp. 466–73.
14. I. Calliari, M. Pellizzari, M. Zanellato, and E. Ramous: *J. Mater. Sci.*, 2011, vol. 46, pp. 6916–24.
15. J. Gao, Y.M. Jiang, B. Deng, W. Zhang, C. Zhong, and J. Li: *Electrochim. Acta*, 2009, vol. 54, pp. 5830–35.
16. I. Calliari, I. Dobranszky, I. Ramous, G. Straffellini, and G. Rebuffi: *6th European Stainless Steel Conference: Science and Market*, Helsinki, 2008, p. 623.
17. M. Perez, C. Sidoroff, A. Vincent, and C. Esnouf: *Acta Mater.*, 2009, vol. 57, pp. 3170–81.
18. V. Massardier, T. Epicier, and P. Merle: *Acta Mater.*, 2000, vol. 48, pp. 2911–24.
19. F.J. Blatt, P.A. Schroeder, and C.L. Foiles: *Thermoelectric Power of Metals*, Plenum Press, New York, 1976.
20. M. Houze, X. Kleber, F. Fouquet, and M. Delnondedieu: *Scripta Mater.*, 2004, vol. 51, pp. 1171–76.
21. R. Borrelly and D. Benkirat: *Acta Metall.*, 1985, vol. 33, pp. 855–66.
22. D. Benkirat, P. Merle, and R. Borrelly: *Acta Metall.*, 1988, vol. 36, pp. 613–20.
23. A.N. Lasseigne, D.L. Olson, H.-J. Kleebe, and T. Boellinghaus: *Metall. Mater. Trans. A*, 2005, vol. 36A, p. 3031.
24. X. Kleber, L. Simonet, and F. Fouquet: *Model. Simul. Mater. Sci.*, 2006, vol. 14, p. 21.
25. T.H. Lee, C.S. Oh, H.N. Han, C.G. Lee, S.J. Kim, and S. Takaki: *Acta Crystall. B*, 2005, vol. 61, pp. 137–44.
26. T.H. Lee, C.S. Oh, C.G. Lee, S.J. Kim, and S. Takaki: *Scripta Mater.*, 2004, vol. 50, pp. 1325–28.
27. H.L. Yakel: *Acta Crystall. B*, 1987, vol. 43, p. 230.
28. M. Calcagnotto, D. Ponge, E. Demir, and D. Raabe: *Mater. Sci. Eng. A*, 2010, vol. 527, pp. 2738–46.
29. D. Qiu and W. Zhang: *Acta Mater.*, 2007, vol. 55, pp. 6754–64.
30. C. Cayron, F. Barcelo, and Y. de Carlan: *Acta Mater.*, 2010, vol. 58, pp. 1395–402.
31. L. Pryce and K. W. Andrews, *J. Iron Steel Inst.*, 1960, p. 415.
32. L. Zhang, W. Zhang, Y. Jiang, B. Deng, D. Sun, and J. Li: *Electrochim. Acta*, 2009, vol. 54, pp. 5387–92.
33. T.H. Lee, H.Y. Ha, B. Hwang, and S.J. Kim: *Metall. Mater. Trans. A*, 2012, vol. 43A, pp. 822–32.
34. C. Cayron: *Acta Crystall. A*, 2013, vol. 69, p. 498.
35. R.D. Knutsen, C.I. Lang, and J.A. Basson: *Acta Mater.*, 2004, vol. 52, pp. 2407–17.
36. H.U. Hong, B.S. Rho, and S.W. Nam: *Mater. Sci. Eng. A*, 2001, vol. 318, pp. 285–92.
37. G.H. Eichelman and F.C. Hull: *Trans. Am. Soc. Met.*, 1953, vol. 45, p. 77.
38. H. Mehrer, ed.: *Landolt-Börnstein New Series Group III: Volume 26: Diffusion in Solids Metals and Alloys*, Springer, Heidelberg, 1990.
39. R.A. Perkins, R.A. Padgett, and N.K. Tunali: *Metall. Trans.*, 1973, vol. 4, p. 2535.
40. A.F. Padilha and P.R. Rios: *Isij Int.*, 2002, vol. 42, pp. 325–37.
41. C.S. Huang and C.C. Shih: *Mater. Sci. Eng. A*, 2005, vol. 402, pp. 66–75.
42. D.A. Porter and K.E. Easterling: *Phase Transformations in Metals and Alloys*, Chapman & Hall, London, 1992.
43. F.G. Caballero, C. Capdevila, L.F. Alvarez, and C.G. de Andres: *Scripta Mater.*, 2004, vol. 50, pp. 1061–66.
44. N.O. Lara, A. Ruiz, C. Rubio, R.R. Ambriz, and A. Medina: *NDT&E Int.*, 2011, vol. 44, pp. 463–68.